Auto-focus by Lissajous scanning in Time-reversal optical scanning holography

Jie Liu (刘 洁)[2], Haiyan Ou (欧海燕)[1,2*], Hua Wang (王 华)[2], Lin Peng (彭 麟)[3] and Wei Shao (邵 维)[1]

[1] School of Physics, The University of Electronic Science and Technology of China, Chengdu 611731, China
[2] Shenzhen Institute for Advanced Study, The University of Electronic Science and Technology of China, Shenzhen 518000, China
[3] Key Laboratory of Cognitive Radio and Information Processing, Guilin University of Electronic Technology, Guilin 541004, China

*Corresponding author: ouhaiyan@uestc.edu.cn

In this manuscript, an auto-focusing method in optical scanning holography (OSH) system is proposed. By introducing Lissajous scanning into multiple signal classification (MUSIC) method in time reversal (TR) OSH, the axial locations of the targets can be retrieved with better resolution and the peak prominence increases from 0.21 to 0.34. The feasibility of this method is confirmed by simulation as well as experiment.

Keywords: digital holography, Lissajous scanning, image reconstruction, axial localization.
DOI: xxxxxxx/COLxxxxxxx.

1. Introduction

Optical scanning holography (OSH) is an incoherent digital holography (DH) technology[1] that has found extensive application in domains including encryption[2,3], 3D display[4], remote sensing[5], and microscopy[6]. In OSH, the amplitude and phase information of the three-dimensional (3D) objects are recorded in two-dimensional (2D) holograms by raster scanning.

Reconstruction is an important process in OSH, which means to retrieve distinct sections of the 3D object from the hologram. ~~The key to reconstruction lies in the prior knowledge of the axial location of each section. This process is also known as auto-focusing.~~ It is generally necessary to use an auto-focusing algorithm to extract the true position of the object from the hologram for reconstructing a focused and sharp image[7].~~Unfortunately, a straightforward analysis of the 2D hologram can not provide the desired depth information.~~

There are a number of pioneering auto-focusing works in OSH[7–11]. Kim and Poon utilise the Wigner distribution to retrieve the depth parameter[12]. Ren et al. put forward an entropy minimization method to achieve auto-focusing[13]. Meanwhile, edge sparsity has also demonstrated its capability to deal with auto-focusing[14].

With the ongoing development in deep learning, neural networks have also been applied to auto-focus in recent years[15–19]. Pitkäaho et al. employ the AlexNet architecture to estimate the focal position, which necessitates hologram preprocessing[20]. Auto-focus is treated as a classification problem and operationalized with deep learning[21]. Despite its high efficacy, this method demands a predefined set of discrete distances, making it inflexible. Madali and co-authors propose two depth information extraction methods based on U-Net architecture[22].

The spatiotemporal focusing characteristics of time reversal can accurately locate objects, making it useful in OSH for addressing auto-focusing[23]. Formerly, we have presented an auto-focusing method using multi-signal classification (MUSIC) based on time-reversal (TR) technique[24]. However, the MUSIC method typically requires point-by-point scanning to achieve high resolution, which can be time-consuming. The diagonal scanning method proposed to improve calculation speed but sacrifices resolution. Therefore, the balance between resolution and auto-focus speed needs to be considered carefully further. In this paper, by incorporating Lissajous scanning into TR-MUSIC, a higher resolution with a reasonable time investment has been achieved.

This manuscript is organized as follows: Section 2 presents the OSH system principle, followed by an explanation of axial localization, i.e. auto-focusing, based on Lissajous scanning theory. In order to highlight the effectiveness of the proposed method, results from both simulation and experimentation are presented in Section 3 and Section 4, respectively. The concluding remarks are provided in Section 5.
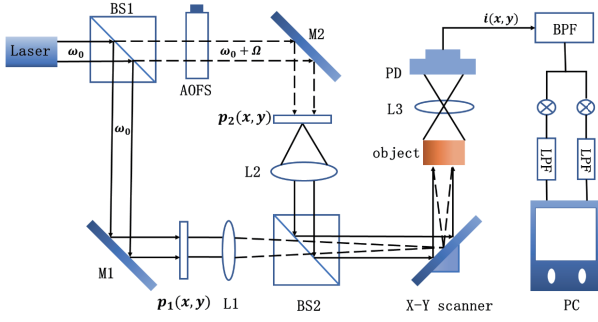
Fig. 1. OSH system. BS, beam splitter; AOFS, acousto-optic frequency shifter; M, mirror; $p(x,y)$, pupil; L, lens; PD, photo-detector; BPF, band-pass filter; LPF, low-pass filter.

2. Principle

2.1. Optical scanning holography

Fig. 1 illustrates an optical scanning holography system[1]. The laser emits a light beam that splits into two at the beam splitter BS1. One of the beams transmits through the mirror M1, the pupil $p_1(x,y)$ and the lens L1. The other beam first undergoes frequency modulation at an acousto-optic shifter (AOFS) before passing through the mirror M2, the pupil $p_2(x,y)$, and then the lens L2. The X-Y scanning mirror reflects the two beams, which converge at the BS2, enabling them to scan the object point by point. The optical signal is transformed into an electrical signal by a photo-detector (PD) following light's passage through lens L3. After demodulation, the electrical signal is stored as a hologram on the computer.

If we discretize the 3D object into N sections along the z-axis, then the complex amplitude of the object can be expressed as $O(x,y;z_i)$, in which x and y are space coordinates, and z_i denotes the distance between the i-th section and the scanning mirrors. In OSH, we choose specifically pupils, where $p_1(x,y) = 1$ (omitting finite size effects) and $p_2(x,y) = \delta(x,y)$, i.e., a Dirac delta function. The spatial impulse response $h(x,y;z)$ can be expressed as[8]

$$h(x,y;z) = (j/\lambda z)exp\left\{(-\pi/NA^2z^2 + j\pi/\lambda z)(x^2+y^2)\right\} \quad (1)$$

where j is the imaginary unit and λ is the wavelength of light. NA stands for the numerical aperture of Gaussian function. Therefore, the hologram can be expressed as

$$g(x,y) = \int_{-\infty}^{\infty} (|O(x,y,z)|^2 \otimes h(x,y;z))dz$$

$$\approx \sum_{i=1}^{N} (|O(x,y,z_i)|^2 \otimes h(x,y;z_i)) \quad (2)$$

where $\otimes$ represents the convolution operation.

The reconstructed image of the l-th layer can be expressed as

$$I_{out}(x,y;z_l) = \sum_{i=1}^{N}(|O(x,y,z_i)|^2 \otimes h(x,y;z_i)) \otimes h^*(x,y;z_l)$$

$$= |O(x,y,z_l)|^2 \otimes \gamma + \sum_{i \neq l}^{N} |O(x,y,z_i)|^2 \otimes h(x,y;z_i)$$

$$\otimes h^*(x.y;z_l) \quad (3)$$

where $\gamma = h(x,y;z_l) \otimes h^*(x.y;z_l)$ and $*$ represents the conjugation operation. The equation consists of two terms: the information image of the focused section and the defocus noise from other sections.

2.2. Time reversal optical scanning holography

TR is a technique to focus wave energy to a selected point in space and time. It can locate targets in turbid media due to its inherent synchronised time and space focusing properties[23,25]. While MUSIC algorithm based on eigenvalue decomposition and subspace theory, can provide high resolution and stability to detect target directions[26,27]. TR-MUSIC is a combination algorithm that merges the adaptive focusing of TR technique with the high resolution of the MUSIC algorithm. It has been widely used in electromagnetic waves, optical waves and other fields[28–32].

In our previous work, it has shown that TR-MUSIC could be adapted to work with digital holography [24]. Due to the reciprocity of light propagation, TR matrices T_{DSSD} and T_{SDDS} in digital holography are formulated. Where T_{DSSD} represents the light propagation from the detector to the light source and back, while T_{SDDS} refers to the reverse propagation of light originating from the source.

The matrix T_{DSSD} can be expressed by means of singular value decomposition (SVD)[33] as

$$T_{DSSD} = \mathscr{F}^{-1}\left\{GG^H\right\}$$

$$= \sum_{m=1}^{M} v_x(m) \cdot |O(x_m,y_m,z_m)|^2 \cdot \|v_y(m)\| \cdot v_x^H(m) \quad (4)$$

where G is the Fourier transform of $g(x,y)$. ^{H} indicates the conjugate transpose operation. $m = 1,2,...,M$. $|\cdot|$ and $\|\cdot\|$ represent the absolute value and modulo operations respectively. The column vectors in x and y directions are denoted as v_x and v_y. T_{SDDS} is constructed as $T_{SDDS} = \mathscr{F}^{-1}\left\{G^HG\right\}$.

If the object has M target points, then the matrix would exhibit M positive eigenvalues, with the other eigenvalues near zero. The primary M vectors of the TR matrix denote the signal subspace, while the remaining vectors correspond to the noise subspace. The connection between them can be expressed as

$$T_{DSSD} \cdot v_x(m) = |O(x_m,y_m,z_m)|^2 \cdot \|v_y(m)\| \cdot \|v_x(m)\| \cdot v_x(m)$$

$$T_{SDDS} \cdot v_y^*(m) = |O(x_m,y_m,z_m)|^2 \cdot \|v_y(m)\| \cdot \|v_x(m)\| \cdot v_y^*(m) \quad (5)$$

where $v_x(m)$ and $v_y(m)$ are the eigenvectors of matrices T_{DSSD} and T_{SDDS} respectively. As previously mentioned, the 3D object is discretized into N layers along the z-axis, with each layer divided into $U \times U$ points. The locations of the targets can be determined through computation.

$$K_x(X_p, z_i) = \sum_{m=M+1}^{U} \left| (v_x(m)^T v_1^*(X_p, z_i)) \right|^2$$

$$K_y(X_p, z_i) = \sum_{m=M+1}^{U} \left| (v_y^*(m)^T v_2(X_p, z_i)) \right|^2 \quad (6)$$

where X_p represents the position of the test point in the $x-y$ plane . $v_1^*(X_p, z_i)$ and $v_2(X_p, z_i)$ are eigenvectors of matrices $G(X_p)G(X_p)^H$ and $G(X_p)^H G(X_p)$, respectively.

When the tested object is in the same position as the actual target, the minimum value of Eq. (6) is achieved due to the orthogonality between the signal and noise subspace.

The pseudo-spectrum $P_x(X_p, z_i)$ and $P_y(X_p, z_i)$ in the x and y directions can be expressed as

$$P_x(X_p, z_i) = \|v_1(X_p, z_i)\|^2 / K_x(X_p, z_i)$$

$$P_y(X_p, z_i) = \|v_2(X_p, z_i)\|^2 / K_y(X_p, z_i) \quad (7)$$

Then the combined pseudo-spectrum becomes

$$P(X_p, z_i) = P_x(X_p, z_i) \cdot P_y(X_p, z_i) \quad (8)$$

We then traverse the test positions in the section at $z = z_i$. The parameters of each layer $P(z_i)$ can be calculated, and the local maxima are considered as the axial locations.

$$P(z_i) = \sum_{p=1}^{U^2} P(X_p, z_i) \quad (9)$$

Typically, all $U \times U$ points of each layer are selected as test positions, resulting in high resolution in MUSIC algorithm. However, this approach can be very time-consuming. As indicated by Eq. (7), one can label the diagonal elements as test points[24]. The target point will always respond at the diagonal position, regardless of its location. For instance, if the object is located at (x_1, y_1), it will generate responses at $x = x_1$, and $y = y_1$. They will intersect the diagonal and produce two response points at (x_1, x_1) and (y_1, y_1). Therefore, we can only calculate the pseudo-spectrum at the diagonal position, reducing computational effort. The diagonal scanning method can be expressed as

$$P(z_i)|_{diagonal} = \sum_{d=1}^{U} P(x_d, y_d, z_i) \quad (10)$$

where $x_d = y_d$, and (x_d, y_d) represents the diagonal position of the test point X_p in the $x-y$ plane. It can be deduced from Eq. (10) that this method significantly reduces computation time. However, it does come at the cost of resolution.
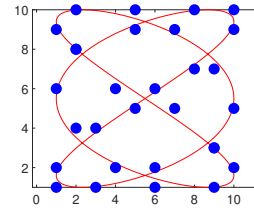

Fig. 2. The Lissajous curve and the selected test positions.

2.3. Lissajous scanning

Considering the limitations of both full and diagonal pseudo spectrum, we introduce here Lissajous scanning as a method for the balance between resolution and auto-focus speed. The two axes in a Lissajous scan possess similar single-tone frequencies. This technology allows the scanning system to operate at resonance, enabling fast, large-amplitude scanning. Especially low power consumption during high quality factor scanning[34]. The Lissajous trajectory technique is utilized in various fields including optical coherence tomography (OCT)[35,36], frequency-modulated gyroscopes[37], and microscopy[38]. The equation for the trajectory can be formulated as follows.

$$\begin{cases} x & = & A_x sin(pt) \\ y & = & A_y sin(qt + \phi) \end{cases} \quad (11)$$

where A represents amplitude, p and q represent frequency, respectively. The subscripts x and y indicate the x and y directions. The term ϕ denotes the phase difference.

As the conventional TR-MUSIC method fails to achieve a balance between time and resolution, we introduce Lissajous scanning to improve this. By selecting test points located on the Lissajous scan curve, better resolution can be achieved with a reasonable amount of time. The process is as follows: (1) Adjust the amplitude ratio of the Lissajous curve to match the size of the section; (2) Calculate the period T of the Lissajous curve based on the values of p and q: $T = 2\pi/gca(p,q)$, where $gca(p,q)$ means calculating the greatest common divisor of p and q; (3) Select V evenly spaced points within the time period from 0 to T to discretize the curve; (4) Follow the nearest neighbor rule to select V units as test positions from the $U \times U$ points of each layer; (5) Use these selected positions as the test points X_p to estimate the depth location of targets.

The Lissajous scanning-based approach delivers greater precision than diagonal element testing and requires fewer computations than point-by-point testing. Fig. 2 shows the Lissajous curve (red line) with a amplitude ratio of $10 : 10$, a frequency ratio of $3 : 2$ and a phase difference of 0. By following the aforementioned steps (1)-(5), the discrete points are generated with $V = 30$ in step (3) as an example. The results are shown by the blue points in Fig. 2.
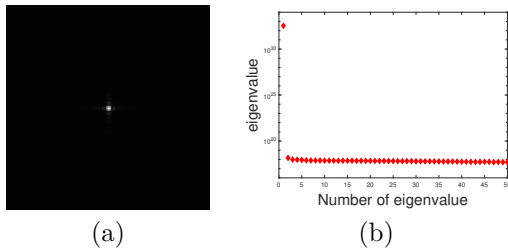
(a)   (b)

Fig. 3. (a) The generated hologram, (b) the first 50 eigenvalues.
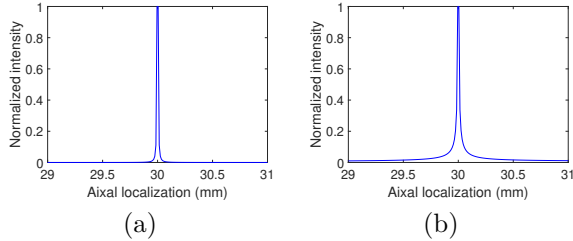

(a)   (b)

Fig. 4. The sum of the pseudo-spectrum along the z-axis, where target at (a) $(10,6)$ and (b) $(30,10)$.

3. Simulation

In this section, we demonstrate the viability of the proposed method by applying it to single-point targets, multi-point targets, as well as complex objects. The computer configuration is AMD Ryzen 5 5600 6-Core Processor @ 3.50 GHz, 32G RAM. Results and discussions can be found in the subsections below.

3.1. Single point target

We test the proposed method using a simple single point object first. The laser wavelength is set to 632.8 nm in the simulation. The size of each section is $1\,\text{mm} \times 1\,\text{mm}$ and is divided into 100×100 pixels. Parameters for the Lissajous trajectory curve include an amplitude ratio of $100 : 100$, a frequency ratio of $13 : 21$, a phase difference of 0. Taking into account both calculation time and resolution, Lissajous scanning is utilized to choose 1000 test locations per layer for simulation, which is ten times the dimension of the matrix.

There are two possible scenarios due to the fact that the Lissajous trajectory does not pass through every unit in the plane. The outcomes could either be that the test points selected using the Lissajous curve encompass the single point target or that they do not encompass it. In the first case, the target points is located at $(10,6)$. While for the second case, the target is at $(30,10)$ with no intersection with the Lissajous trajectory.

The generated hologram and the first 50 eigenvalues of the TR matrix are shown in Fig. 3(a) and (b), respectively. It is apparent that there is only one significant eigenvalue, denoting a single target in the signal subspace.

Fig. 4(a) and (b) show the peak values, indicating that the axial position of the detected object is at 30 mm
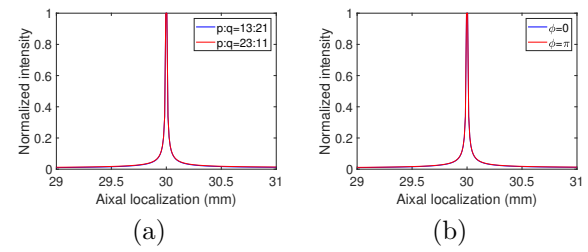

(a)   (b)

Fig. 5. The sum of the pseudo-spectrum along the z-axis (a) frequency ratio $p : q = 13 : 21$ or $p : q = 23 : 11$, and (b) phase difference $\phi = 0$ or $\phi = \pi$.

Table 1. Different frequency ratios in Lissajous curve.

$p : q$	$3 : 2$	$4 : 5$	$9 : 8$	$13 : 21$	$19 : 23$	$23 : 11$
time(s)	33.69	35.24	35.87	31.09	34.91	31.13
FWHM	0.01	0.01	0.01	0.01	0.01	0.01

for both cases. The axial location of the target can be detected regardless of whether the chosen test points of the Lissajous trajectory curve pass through the target point.

When analyzing the proposed method, it is important to consider not only the position of the test point but also the amplitude ratio, frequency ratio, and phase difference of the Lissajous curve. The amplitude ratio is an adjustable factors in the Lissajous curve that depends on the size of the section. Based on Eq. (11), modifications to the frequency ratio and phase difference also affect the trajectory. In the simulation, the test point is located at $(20,5)$ in the $x - y$ plane and 30 mm along the z-axis. The sum of the pseudo-spectrum along the z-axis with different frequency ratios and phase difference are shown in Fig. 5(a) and (b). One can observe from the figure that the calculated axial location is 30 mm under different scenarios, which is consistent with the simulation.

Table 1 and Table 2 present the calculation time and full width at half maximum (FWHM) results with different frequency ratios and phase differences, respectively. FWHM is defined as the distance between two points on the sum of the pseudo-spectrum curve where the function reaches half of its maximum value. As the FWHM value decreases, the peak becomes sharper and the local maximum that needs to be found becomes more prominent. It can be seen from the results that variations in frequency ratios or phase differences do not noticeably affect the outcome of axial localization, with only a marginal impact on calculation time.

Table 2. Different phase differences in Lissajous curve.

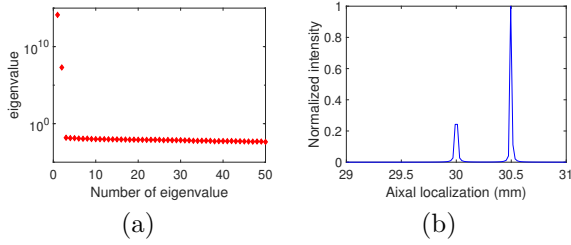| ϕ	0	$\pi/4$	$\pi/2$	$3\pi/4$	π	$3\pi/2$
time(s)	31.25	41.59	41.69	42.23	31.22	41.24
FWHM	0.01	0.01	0.01	0.01	0.01	0.01

Fig. 6. (a) The first 50 eigenvalues of TR matrix, (b) the sum of the pseudo-spectrum along the z-axis.
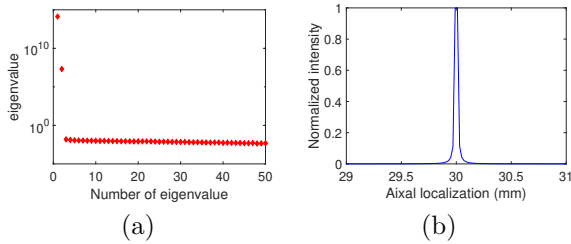

Fig. 7. (a) The first 50 eigenvalues of TR matrix, (b) the sum of pseudo-spectrum of each layer along the z-axis.

3.2. Multi-point target

Multi-point targets include two situations: multiple points on the same plane and multiple points on different planes. This subsection provides simulations for both situations.

First, we simulate the situation where multiple points are in different layers, with each layer containing only one point. In the simulation, one of the points is placed at $(10,6)$ in the $x-y$ plane with $z_1 = 30\,\text{mm}$ in the z-axis, while the other point is at $(10,6)$ with $z_2 = 30.5\,\text{mm}$.

Fig. 6(a) shows the distribution of the first 50 eigenvalues. It can be observed that there are two prominent eigenvalues, indicating that there are two targets. The pseudo-spectrum accumulated along the z-axis is displayed in Fig. 6(b). The two local maxima represent the calculated positions of the two targets: $z_1 = 30\,\text{mm}$ and $z_2 = 30.5\,\text{mm}$. These values are consistent with the actual positions.

Then, we simulate the situation where multiple points are situated on the same layer. Firstly, we will analyse two points: one locates at $(10,6)$ and the other is at $(13,12)$. Both points are at the same axial position of $30\,\text{mm}$.The distribution of the first 50 eigenvalues is shown in Fig. 7(a). One can observe that there are two target points. A local maximum can be observed at $z = 30\,\text{mm}$ in Fig. 7(b), which indicates the axial location of the targets.
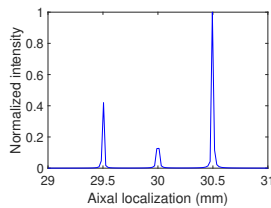

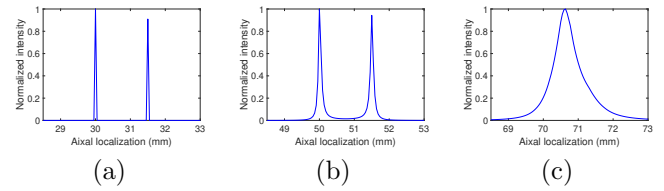**Fig. 8.** The sum of pseudo-spectrum of each layer along the z-axis.

Fig. 9. The sum of pseudo-spectrum along the z-axis (a) $z_1 = 30\,\text{mm}$, $z_2 = 31.5\,\text{mm}$, (b) $z_1 = 50\,\text{mm}$, $z_2 = 51.5\,\text{mm}$, (c) $z_1 = 70\,\text{mm}$, $z_2 = 71.5\,\text{mm}$.
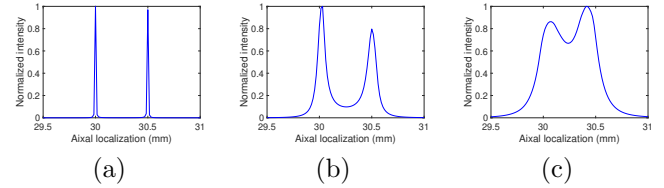
Fig. 10. The sum of pseudo-spectrum along the z-axis (a) $\lambda = 405\,\text{nm}$, (b) $\lambda = 780\,\text{nm}$, (c) $\lambda = 980\,\text{nm}$.

We then consider a more complex situations involving multi-point targets: with one target at $z_1 = 29.5\,\text{mm}$, two at $z_2 = 30\,\text{mm}$, and three targets at $z_3 = 30.5\,\text{mm}$. The result is shown in Fig. 8. It can be observed that there are three local maxima with axial location at $29.5\,\text{mm}$, $30\,\text{mm}$, and $30.5\,\text{mm}$, which match perfectly with the actual case. This demonstrates the feasibility of the proposed approach.

3.3. Resolution analysis

In this section, the resolution analysis of the proposed method is presented. As the TR matrix is based on the hologram. The axial resolution of the proposed methods depends highly on several factors that are crucial to hologram, including the distance of the target as well as the wavelength of light.

We analyze the relationship between the resolution and target distant first. In the simulation, two point targets at $(10,6)$ in the $x-y$ plane with different axial locations are considered. The two targets are kept $1\,\text{mm}$ apart along the z-axis. The results are shown in Fig. 9(a)-(c), with z_1 at $30\,\text{mm}$, $50\,\text{mm}$, and $70\,\text{mm}$, respectively. It can be deduced from Fig. 9 that the resolution degrades as we gradually moves the targets away from the scanning mirror. When the object gets too far away, the method fails to distinguish the two points apart, as is shown in Fig. 9(c).

The impact of laser wavelength on axial resolution is also considered. In the simulation, two point targets are used as the former case, with $z_1 = 30\,\text{mm}$ and $z_2 = 30.5\,\text{mm}$. The calculated sum of pseudo-spectrum along the z-axis with wavelength at $405\,\text{nm}$, $780\,\text{nm}$, and $980\,\text{nm}$ are shown in Fig. 10(a)-(c), respectively. It can be observed from the figure that the two local maxima become less distinct as longer wavelengths are used. This indicates that the axial resolution reduces as the wavelength increases.
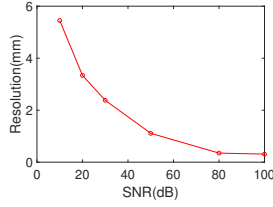
Fig. 11. The relationship between SNR and resolution.

3.4. Noise analysis

In this subsection, the impacts of noise on the proposed method will be evaluated via simulation with different signal-to-noise ratios (SNR). The two test points are both located at $(10,6)$ on the $x-y$ plane but with different axial positions. One of the test points is fixed at the axial position of 30 mm. Gaussian white noise is added to the generated hologram in the simulation. The SNR can be calculated by

$$SNR = 10 \times log_{10}\left(\frac{(\frac{1}{RC}\sum_{r=1}^{R}\sum_{c=1}^{C}F(r,c))^2}{\frac{1}{RC}\sum_{r=1}^{R}\sum_{c=1}^{C}(F(r,c)-F_n(r,c))^2}\right) \quad (12)$$

where R and C stand for the number of rows and the number of columns of the matrix, respectively. F represents the original image, while F_n represents the image with noise.

The relationship between the two variables is shown in Fig. 11. As can be expected, the resolution gets better with higher SNR: when SNR increased from 10 dB to 100 dB, the resolution will change from 5.45 mm to 0.31 mm.

3.5. Complex objects

In this section, the proposed method will be verified through simulation using complex objects. The laser wavelength is set to 632.8 nm. During the simulation, each section of the complex graphics has a size of 1 mm × 1 mm, and is standardised to 128 × 128 pixels, as are shown in Fig. 12(a) and (b). The axial positions of each section are $z_1 = 30$ mm and $z_2 = 35$ mm, respectively. The frequency ratio and phase difference of the Lissajous trajectory are 13 : 21 and 0, respectively. Similarly, the number of test positions per layer is selected to be ten times the dimension of the matrix, which is 1280.

The hologram in Fig. 13(a) was generated based on Eq. (2). The the distribution of eigenvalues is shown in
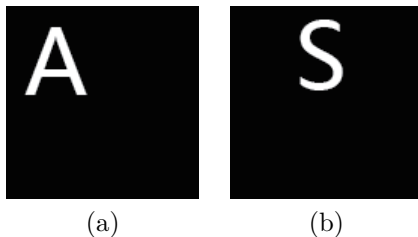

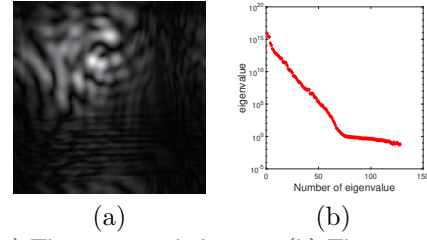**Fig. 12.** Complex objects (a) at $z_1 = 30$ mm and (b) at $z_2 = 35$ mm.

Fig. 13. (a) The generate hologram, (b) The eigenvalues of TR matrix.
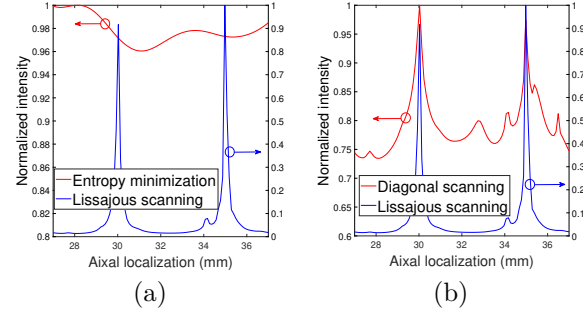

Fig. 14. The proposed method is compared with various positioning methods (a) entropy minimization, (b) TR-MUSIC based on diagonal elements.

Fig. 13(b). One can observe that there are lots of eigenvalues in the signal space for the complex objects. Here, we use L-curve method to partition the signal space[39].

Fig. 14(a) shows the comparison of the TR-MUSIC method using Lissajous scanning (blue line) and the entropy minimization method (red line)[13]. The two local maxima of the proposed method are much more clear compared to the entropy minimization method. ~~It also attains smaller FWHM and interference than the method using diagonal elements, as are shown in Fig. 14(b).~~

Fig. 14(b) shows the axial positioning results of the Lissajous and diagonal scanning methods. It should be noted that the minimum value of the normalized curve obtained through the diagonal scanning method is greater than 0.5. Therefore, the FWHM cannot be calculated. Here we use peak prominence (PP) to measure the prominence of local peak [40]. The PP can be defined as

$$PP = \frac{(L_{max}(S_1)-L_{min}(S_1))+(L_{max}(S_2)-L_{min}(S_2))}{Max-Min} \quad (13)$$

where $L_{max}(S_1)$ and $L_{max}(S_2)$ represent the local maximum value at the first section (S_1) and the second section (S_2) of the object, respectively. $L_{min}(S_1)$ and $L_{min}(S_2)$ represent the nearest local minimum value corresponding to $L_{max}(S_1)$ and $L_{max}(S_2)$. The terms Max and Min respectively represent the maximum value and minimum value in the curve.

Table 3. Performance comparison in simulation.

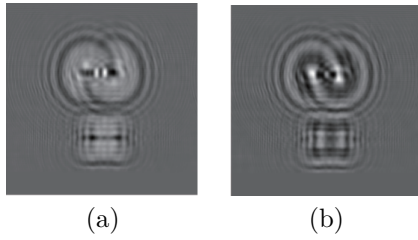| method	entropy	diagonal scan	Lissajous scan
time(s)	0.3	3.8	35.5
PP	*failed*	1.47	1.96

(a)   (b)

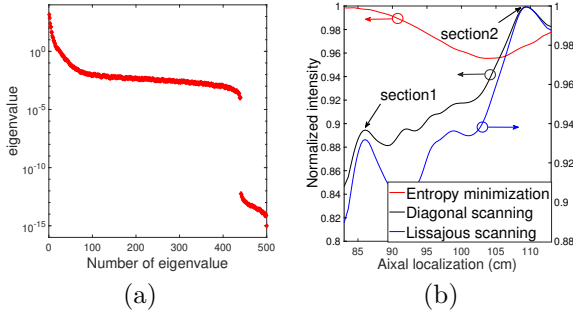**Fig. 15.** The recorded hologram, (a) real part, (b) imaginary part.

(a)   (b)

Fig. 16. (a) The eigenvalues of TR matrix, (b) parameters calculated along the z-axis obtained by different methods.

Fig. 14 and Table 3 indicate~~This indicates~~ that the proposed method outperforms the other two algorithm in dealing with complex objects.

4. Experiments

In this section, we ~~experimentally~~ verify the proposed axial localization method based on Lissajous scanning using real hologram, which was retrieved experimentally by T. Kim[8]. The laser wavelength used in the experiment is 632.8 nm. The diameter of the collimated beam is $D = 25$ mm, and the focal length of the lens is $f = 500$ mm. Thus, $NA \approx D/(2f) = 0.025$. The two sections of the object, sampled with a size of 500×500 pixels, are situated at distances of $z_1 = 87$ cm and $z_2 = 107$ cm.

The proposed method utilises a Lissajous trajectory with a frequency ratio of $13 : 21$ and a phase difference of 0. The number of test locations in each layer is set to ten times the matrix dimension, which is 5000. Fig. 15(a) and (b)[8] are the real part and imaginary part of the hologram, respectively.

The eigenvalues of the TR matrix is shown in Fig. 16(a). The calculated results along the z-axis are presented in Fig. 16(b), with the red curve representing the entropy minimization method, and the black and blue one standing for the diagonal and the proposed method, respectively. During the experiment, the entropy minimization method took 1.1 seconds, but the positioning was unsuccessful.

Table 4. Performance comparison in experiment.

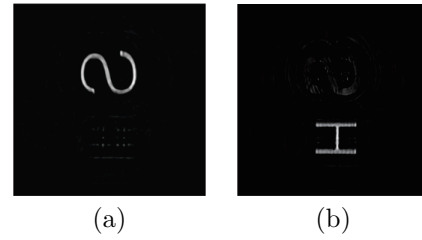| method	entropy	diagonal scan	Lissajous scan
time(s)	1.1	218.5	2281.7
PP	*failed*	0.21	0.34

(a)   (b)

Fig. 17. Reconstructed image at (a) z_1, and (b) z_2.

Table 4 presents the calculation time and PP for both the diagonal scanning method and the Lissajous scanning method. The Lissajous scanning method calculates the position of each layer to be ten times that of the diagonal method. The actual calculation time is consistent with this relationship.

One can observe that the entropy minimization method fail to retrieve the axial location of the two sections. While the results of the other two methods show consistent localization, but the proposed method at $z_1 = 86$ cm and $z_2 = 109$ cm is more prominent.

The reconstruction results based on the calculated axial location of the two sections are listed in Fig. 17(a) and (b) using the inverse imaging method[41]. Experiment results demonstrated that the axial localization method based on Lissajous scanning in time-reversal OSH can achieve accurate positioning of objects.

5. Conclusions

Accurate axial localization is of utmost importance when reconstructing holograms in OSH. Based on the TR-MUSIC algorithm, the Lissajous trajectory curve is introduced to obtain effective test points, through which a better auto-focus resolution has been achieved. The feasibility of this method was verified through simulations as well as experiments. Compared to both entropy minimization algorithm and the diagonal algorithm, the proposed method demonstrated higher resolution and a more optimal balance between resolution and auto-focus time investment.

6. Funding

References

1. T.-C. Poon, *Optical Scanning Holography with MATLAB* (Spring, 2007).
2. T.-C. Poon, T. Kim, and K.Doh, "Optical scanning cryptography for secure wireless transmission," Appl. Opt. **42**, 6496(2003).

3. L.-Z. Zhang, X. Zhou, D. Wang, N.-N. Li, X. Bai, and Q.-H. Wang, "Multiple-image encryption based on optical scanning holography using orthogonal compressive sensing and random phase mask," Opt. Eng. **59**,(2020).

4. E. J. Lee and T. Kim, "Optical scanning holography for a three-dimensional equal scale display," Opt. Express **30**, 8165(2022).

5. B. W. Schilling and G. C. Templeton, "Three-Dimensional remote sensing by optical scanning holography," Appl. Opt. **40**, 5474(2001).

6. E. Y. Lam, X. Zhang, H. Vo, T.-C. Poon, and G. Indebetouw, "Three-dimensional microscopy and sectional image reconstruction using optical scanning holography," Appl. Opt. **48**, H113(2009).

7. Z. Ren, N. Chen, and E. Y. Lam, "Automatic focusing for multisectional objects in digital holography using the structure tensor," Opt. Lett. **42**, 1720(2017).

8. X. Zhang, E. Y. Lam, T. Kim, Y. S. Kim, and T.-C. Poon, "Blind sectional image reconstruction for optical scanning holography," Opt. Lett. **34**, 3098(2009).

9. S. Oh, C.-Y. Hwang, I. K. Jeong, S.-K. Lee, and J.-H. Park, "Fast focus estimation using frequency analysis in digital holography," Opt. Express **22**, 28926(2014).

10. H. Ou, Y. Wu, E. Y. Lam, and B.-Z. Wang, "New autofocus and reconstruction method based on a connected domain," Opt. Lett. **43**, 22201(2018).

11. Z. Xin, K. Dobson, Y. Shinoda, and T.-C. Poon, "Sectional image reconstruction in optical scanning holography using a random-phase pupil," Opt. Lett. **35**, 2934(2010).

12. T. Kim and T.-C. Poon, "Autofocusing in optical scanning holography," Appl. Opt. **48**, H153(2009).

13. Z. Ren, N. Chen, A. Chan, and E. Y. Lam, "Autofocusing of optical scanning holography based on entropy minimization," in *Digital Holography and Three-Dimensional Imaging*, (Optical Society of America, 2015), pp. DT4A-4.

14. Y. Zhang, H. Wang, Y. Wu, M. Tamamitsu, A. Ozcan, "Edge sparsity criterion for robust holographic autofocusing," Opt. Lett. **42**, 3824(2017).

15. Z. Ren, Z. Xu, and E. Y. Lam, "Learning-based nonparametric autofocusing for digital holography," Optica **5**, 337(2018).

16. T. Shimobaba, T. Kakue, and T.Ito, "Convolutional neural network-based regression for depth prediction in digital holography," in *2018 IEEE 27th International Symposium on Industrial Electronics (ISIE)*, (2018), pp. 1323-1326.

17. Y. Wu, Y. Rivenson, Y. Zhang, Z. Wei, H. Günaydin, X. Lin, and A. Ozcan, "Extended depth-of-field in holographic imaging using deep-learning-based autofocusing and phase recovery," Optica **5**, 704(2018).

18. T. Pitkäaho, A. Manninen, and T. J. Naughton, "Focus prediction in digital holographic microscopy using deep convolutional neural networks," Appl. Opt. **58**, A202(2019).

19. L. Huang, T. Liu, X. Yang, Y. Luo, Y. Rivenson, and A. Ozcan, "Holographic image reconstruction with phase recovery and autofocusing using recurrent neural networks," ACS Photonics **8**, 1763(2021).

20. T. Pitkäaho, A. Manninen, and T. J. Naughton, "Focus classification in digital holographic microscopy using deep convolutional neural networks," in *Advances in Microscopic Imaging*, (Optica Publishing Group, 2017), p. 104140K.

21. Z. Ren, Z. Xu, and E. Y. Lam, "Autofocusing in digital holography using deep learning," in *Three-Dimensional and Multidimensional Microscopy: Image Acquisition and Processing XXV*, vol. 10499 (Spie, 2018), pp. 157-164.

22. N. Madali, A.Gilles, P. Gioia, and L. Morin, "Automatic depth map retrieval from digital holograms using a deep learning approach," Opt. Express **31**, 4199(2023).

23. M. Fink, "Time reversal acoustics," Reports on Prog. Phys. **50**, 34(1997).

24. H. Ou, Y. Wu, E. Y. Lam, and B.-Z. Wang, "Axial localization using time reversal multiple signal classification in optical scanning holography," Opt. Express **26**, 3756(2018).

25. B. Wu, M. Alrubaiee, M. Xu, S. K. Gayen, and W. Cai, "Time reversal optical tomography: locating targets in a highly scattering turbid medium," Opt. Express **19**, 21956(2011).

26. X. Chen and Y. Zhong, "A robust noniterative method for obtaining scattering strengths of multiply scattering point targets," J. Acoust. Soc. Am. **122**, 1325(2007).

27. X. Chen and K. Agarwal, "MUSIC algorithm for two-dimensional inverse problems with special characteristics of cylinders," IEEE Trans. on Antennas Propag. **56**, 1808(2008).

28. A. J. Devaney, E. A. Marengo, and F. K. Gruber, "Time-reversal based imaging and inverse scattering of multiply scattering point targets," J. Acoust. Soc. Am. **118**, 3129(2005).

29. E. A. Marengo, F. K. Gruber, and F. Simonetti, "Time-reversal music imaging of extended targets," IEEE Trans. on Image Process. **16**, 1967(2007).

30. X.-F. Liu, B.-Z. Wang, and J. L.-W. Li, "Transmitting-mode time reversal imaging using music algorithm for surveillance in wireless sensor network," IEEE Trans. on Antennas Propag. **60**, 220(2012).

31. D. Ciuonzo, G. Romano, and R. Solimene, "Performance analysis of time-reversal music," IEEE Trans. on Signal Process. **63**, 2650(2015).

32. M. Kafal and A. Cozza, "Multifrequency TR-MUSIC processing to locate soft faults in cables subject to noise," IEEE Trans. on Instrum. Meas. **69**, 411(2020).

33. K. Dan, "A singularly valuable decomposition: The svd of a matrix," Coll. Math. J. **27**, 2(1996).

34. D. Brunner, H. W. Yoo, R. Schroedter, and G. Schitter, "Adaptive Lissajous scanning pattern design by phase modulation," Opt. Express **29**, 27989(2021).

35. Y. Chen, Y.-J. Hong, S. Makita, and Y. Yasuno, "Three-dimensional eye motion correction by Lissajous scan optical coherence tomography," Biomed. Opt. Express **8**, 1783(2017).

36. S. Makita, S. Azuma, T. Mino, T. Yamaguchi, M. Miura, and Y. Yasuno, "Extending field-of-view of retinal imaging by optical coherence tomography using convolutional Lissajous and slow scan patterns," Biomed. Opt. Express **13**, 5212(2022).

37. M. Leoncini, M. Bestetti, A. Bonfanti, S. Facchinetti, P. Minotti, and G. Langfelder, "Fully integrated, 406 μA, 5 °/hr, full digital output Lissajous frequency-modulated gyroscope," IEEE Trans. on Ind. Electron. **66**, 5212(2019).

38. N. O. Loewke, Z. Qiu, M. J. Mandella, R. Ertsey, A. loewke, L. A. Gunaydin, E. L. Rosenthal, C. H. Contag, and O. Solgaard, "Software-based phase control, video-rate imaging, and real-time mosaicing with a Lissajous-scanned confocal microscope," IEEE Trans. Med. Imaging **39**, 1127(2020).

39. B. Wu, W. Cai, M. Alrubaiee, M. Xu, and S. K. Gayen, "Three dimensional time reversal optical tomography," in *SPIE BiOS*, (2011), PP. 242-243.

40. B. Cox, L. Van der Perre, S. Wielandt, G. Ottoy, and L. De Strycker, "High precision hybrid RF and ultrasonic chirp-based ranging for low-power IoT nodes," EURASIP J. Wirel. Commun. Netw. **2020**, 1(2020).

41. X. Zhang, E. Y. Lam, and T.-C. Poon, "Reconstruction of sectional images in holography using inverse imaging," Opt. Express **16**, 17215(2008).